J. Fluid Mech. (1987), *vol.* 183, *pp.* 235–263
Printed in Great Britain

Near-surface turbulence in a grid-stirred tank

By BLAIR H. BRUMLEY
Woods Hole Oceanographic Institution, Woods Hole, MA 02543, USA

AND GERHARD H. JIRKA
DeFrees Hydraulics Laboratory, Cornell University, Ithaca, NY 14853, USA

(Received 21 April 1986 and in revised form 16 March 1987)

In order to elucidate the turbulent structure below a shear-free gas–liquid interface, turbulence measurements were made in a 50 cm square by 40 cm deep tank stirred by a vertically oscillating grid well below the surface, using a split-film anemometer probe rotating in a horizontal circle. This instrument is able to measure both vertical and horizontal velocity fluctuations to within 0.4 mm of the surface, from which spatial spectra and profiles of r.m.s. velocity fluctuations and integral lengthscales can be calculated. The turbulent structure is affected by the presence of the surface within a 'surface-influenced layer' roughly one integral scale, or ten per cent of the distance from the surface to the centre of the grid stroke, in thickness. The shapes of the spectra and profiles within the surface-influenced layer are predicted to a good first approximation by the source theory of Hunt & Graham (1978), which treats the turbulent structure as the superposition of homogeneous turbulence with an irrotational velocity field driven by a source distribution at the surface which cancels the vertical velocity fluctuations there. The magnitudes (as opposed to the shapes) of the profiles scale according to the values that would otherwise occur in the vicinity of the surface-influenced layer were the surface not present. These magnitudes are adequately predicted by the bulk relations determined by Hopfinger & Toly (1976) and Thompson & Turner (1975), with no apparent dependence on turbulent Reynolds number. There are some minor discrepancies between the measured profiles and those of Hunt & Graham. A thin layer of reduced velocity fluctuations below what would be expected from the theory was observed near the surface. Also, anisotropy in the velocity spectra at depths within the surface-influenced layer extended well into the inertial subrange, whereas the Hunt & Graham theory predicts no anisotropy at high wavenumbers.

1. Introduction

Grid-stirred tank experiments afford a unique opportunity to study the modification and distortion of free fluid turbulence by an essentially shear-free surface, as provided by the gas–liquid interface of the tank. The grid-stirred tank with a free surface is thus a simple and readily controllable analogue for the approach of bottom-generated turbulence toward the free surface, as is typical in environmental systems (e.g. rivers, estuaries) and industrial processes (e.g. mixing channels, stripping columns). The mechanics of the near-surface turbulence are the key element in transfer and diffusion processes in such systems due to their intricate interaction with time-dependent mass or heat boundary layers that exist at the interface. Improved predictive formulations for surface transfer processes as well as better

specifications of 'surface functions' (mimicking the sub-grid details) for general turbulence models all require detailed knowledge of the structure of the near-surface turbulence.

Of the extensive literature concerned with turbulent boundary layers, surprisingly little concerns free (or for that matter solid) surfaces with zero mean shear stress. Perhaps this is because the focus of boundary-layer research is most often on turbulence generated by the boundary layer itself. There is no such source of turbulence in the zero mean shear case, leaving only the secondary phenomenon of the more passive effect of the kinematic boundary condition imposed by the surface on ambient turbulence generated elsewhere.

The boundary conditions at a free surface differ from those at a solid boundary in two ways, even when there is zero mean shear stress on each. First, the surface is free to move in the normal (vertical) direction, the constraints of gravity and surface tension allowing surface waves to occur. Since the distortion of the turbulent velocity field by the wave velocity field has no significant dynamic effect under the conditions of low to moderate wave slope treated here, the surface may be idealized as being flat (Hunt 1984*a*). Secondly, instead of the no-slip condition on tangential velocity components, there is the condition that the instantaneous shear-stress fluctuations at the surface on the water side must balance the surface gradient of the surface tension (zero for a clean isothermal surface) and the air-side shear-stress fluctuation (negligible for calm air since both the density and the dynamic viscosity are much less than those of water).

Hunt & Graham (1978) (hereinafter HG) developed a theory to account for wind-tunnel measurements of grid-generated turbulence near a solid wall formed by a belt moving at the mean wind speed. The no-slip condition for velocity fluctuations parallel to the wall creates a thin viscous boundary layer that grows slowly with distance down the wind tunnel. Outside this viscous layer is a region roughly one integral lengthscale thick called the 'source layer' because it can be regarded as the superposition of the far-field turbulent velocity field on an irrotational field driven by a source-like distribution on the wall to cancel the perpendicular velocity fluctuations there. HG calculated one-dimensional velocity spectra and velocity fluctuation profiles by applying their superposition theory to isotropic homogeneous high-Reynolds-number turbulence in the far field. The effect of the surface is most striking for the transverse spectrum of the normal velocity component where suppression of eddies larger than the depth y causes a reduction and flattening of the spectrum at wavenumbers below $1/y$. The longitudinal spectrum of the tangential velocity component, on the other hand, only shows a small increase at wavenumbers between $1/L_\infty$ and $1/y$, where L_∞ is the integral lengthscale. Simple numerical approximations to the HG profile predictions are presented in the Appendix. These predictions compared favourably with measurements by Thomas & Hancock (1977) of normal turbulent velocities near a moving wall but less well for transverse components.

Hunt (1984*a*) claimed that the HG source-layer solution can be directly applied to a flat gas–liquid interface. The viscous boundary layer is somewhat different from that in the wind tunnel, however, because it develops to a steady-state thickness and because the boundary condition for horizontal velocity fluctuations is different. The thickness of the viscous boundary layer can be estimated to be smaller than the integral lengthscale by a factor equal to the square root of the turbulent Reynolds number. If the surface is 'clean', that is, truly shear-free, the effect on an eddy of the absence of shear-stress fluctuations at the surface is a small change in the

magnitudes of the horizontal velocity – owing to the zero gradient at the surface – and a small reduction of the surface divergence. If the surface is 'dirty' (owing to contamination often present in nature and most experiments) and can support fluctuating shear stresses, it behaves in the extreme like a solid wall, making the horizontal velocity and the surface divergence both zero so that the instantaneous vertical velocity varies as the square of the distance from the surface at small distances (Hunt 1984*a*).

As a related experiment, McDougall's (1979) measurements of vertical and horizontal velocity fluctuation profiles near a horizontal solid plate located above an oscillating grid were in general agreement with the HG theory. However, the predicted amplification very close to the plate of the horizontal velocity fluctuations could not be observed, apparently owing to the presence of a viscous boundary layer of thickness in rough agreement with the above Hunt (1984*a*) value. A further discussion of the HG theory and its applicability to McDougall's experiment and other flow configurations is given in Hunt (1984*b*).

A number of grid-stirred experiments have been carried out with the objective of mapping the turbulence in the bulk of a homogeneous fluid far from free or solid boundary surfaces (e.g. Thompson & Turner 1975; Hopfinger & Toly 1976; Dickenson & Long 1978; McDougall 1979). These studies demonstrated a linear increase of the horizontal integral lengthscale L_u with distance from a vertical origin at approximately the centre of the grid stroke

$$L_u = az. \tag{1}$$

Thompson & Turner (1975, hereinafter TT) found the constant a to be of order 0.1, while Hopfinger & Toly (1976, hereinafter HT) found 0.15–0.35, as a function of mesh size and stroke. Based on their own and on the TT measurements, HT proposed a dimensionally consistent relation for the horizontal velocity fluctuation u'

$$u' = 0.25 f S^{1.5} M^{0.5} z^{-1}, \tag{2}$$

in which S is the grid stroke (peak-to-peak) and M the grid mesh size. Equations (1) and (2) give a depth-independent turbulent Reynolds number $R_L = u'(2L_u)/\nu$ in the bulk of the fluid, in which ν is the kinematic viscosity. This constancy has been discussed by Long (1978) using the concept of the grid action $K = u'L_u$ as the only dynamically significant parameter of the grid-generation mechanism in the far field. An earlier equation for u' suggested by TT that contained a $z^{-1.5}$ dependence is now considered unreliable (HT; McDougall 1979) as TT attempted to include data for high-solidity perforated-plate experiments for which the Reynolds number is not depth-independent. Few measurements on vertical velocity fluctuations w' have been conducted. HT report anisotropies w'/u' of order of 1.1–1.3 at sufficient distances from the grid, while McDougall found about 1.4. McDougall also detected significant horizontal non-uniformities of turbulence intensities and mean circulations in his tank, a feature apparently more or less common to all stirred grid experiments.

The only other turbulence measurements near the free surface of a grid-stirred tank known to us were made by Dickey *et al.* (1984). They simultaneously measured vertical and horizontal velocity fluctuations as well as the directionally averaged integral lengthscale by digitizing streak photographs taken with vertical slit illumination from the side of the tank. They found surface effects, such as anisotropy in velocity fluctuations and departure of the integral lengthscale from a linear profile, within 1–2 integral lengthscales from the free surface.

This paper reports detailed measurements of the turbulence structure in a

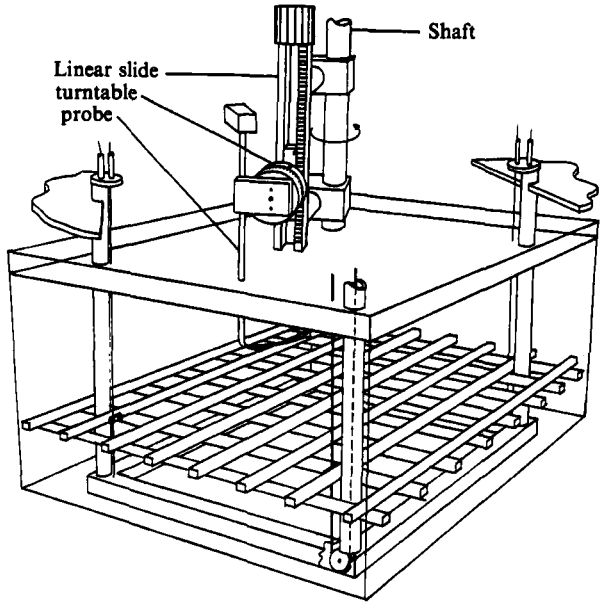

FIGURE 1. Schematic of grid-stirred tank. Interior dimensions of tank are 50 cm square by 40 cm deep. The probe rotates in a 1.00 m circumference horizontal circle concentric with the tank walls. The shaft and grid guides are supported by a surrounding tower (not shown).

grid-stirred tank experiment with emphasis on the near-surface structure. Vertical and horizontal velocities were measured using a rotating split-film hot-film probe.

The experimental data are compared with profiles derived from earlier work; the experimental results of TT and HT are used to predict the conditions that would have occurred were no surface present, while the theoretical results of HG are used to predict the modification of the turbulent structure by the presence of the surface.

2. Experiment

2.1. *Grid-stirred tank*

The experiment was performed in a 0.50 m square tank 0.40 m deep (see figure 1), having a frame made of welded steel angle, with glass front, back and bottom panels for optical clarity and Plexiglas side panels to allow ports to be installed. The tank is designed to be isolated as much as possible from sources of vibration to minimize the generation of surface waves and allow measurements close to the surface. A tower, also of welded steel angle, stands over the tank on separate legs to hold the grid stirrer frame (suspended within the tank, but not connected to it in any way) and the rotating probe holder and instrument platform. An 8×8 grid of 13 mm square bars spaced at 63.5 mm on centre is suspended on four 1.6 mm wire rope cables so as to slide up and down with the grid frame as a guide. This grid is of similar dimensions and the same solidity of 0.36 (i.e. it covers 36 % of the plan area) as those of TT, HT and McDougall (1979). The walls form planes of symmetry with respect to the mesh pattern to minimize secondary circulations as recently discussed by E & Hopfinger (1986). The cables pass over blocks (pulleys) at the bottom of the grid frame and up through the insides of the four vertical guide tubes. They form four continuous loops that are connected via flexible sleeves to a linear slide on a motor-crank assembly

mounted on the wall adjacent to the top of the tower. This arrangement minimizes the transmission of vibrations from the grid-stirring motor to the tower. Adjustments in motor speed and the crank pin on the motor flywheel assembly allow a range of grid frequencies between 0.5 and 5 Hz and of peak-to-peak strokes between 13 and 150 mm.

2.2. *Rotating split-film anemometer*

The probe support and instrument platform are supported by a hollow vertical shaft mounted with ball bearings on the tower. A linear slide, graduated to 0.01 mm to allow precise vertical positioning of the probe, is mounted on an arm so that the probe travels in a 1.00 m circumference horizontal circle. A turntable connecting the probe clamp to the slide allows the probe angle to be adjusted for calibration purposes. Twelve silver slip rings are mounted near the top of the shaft to provide signal and d.c. power connections to the instruments.

A universal-joint coupling connects the shaft without gearing to a d.c. motor at the top of the tower. A seven-pole tachometer geared at 40:130 to the motor shaft provides a feedback signal for the motor controller. The controller follows the 3% peak-to-peak tachometer ripple causing a periodic component to horizontal velocity measurements that appears as narrow spikes in the velocity spectrum at the pole frequency and its second harmonic. These spikes can easily be detected and removed. An incremental encoder mounted on top of the motor provides a 2048-pulse-per-turn square wave and a single index pulse to allow measurement of probe speed and coordination of signal digitization with probe position.

A custom-built split hot-film probe (TSI model 1287AD) with two 1.3 mm sensing-length quartz-coated platinum films at the top and bottom of a 0.15 mm diameter cylindrical quartz fibre allows measurement of horizontal (in the direction of probe travel) and vertical velocity fluctuations. The sensor is mounted on an L-shaped probe that slopes upward at a 5° angle so that the surface can be approached from below without disturbance, and is curved along the circular probe path to minimize its wake. The probe is connected with short coaxial cables to two constant-temperature anemometer amplifiers (TSI model 1750) mounted on the rotating instrument platform. The two anemometer signals are each connected via the slip rings to a filter/programmable-gain amplifier/multiplexer/14-bit A-D converter unit (Neff system 620, series 100). The Neff unit is connected by a 16-bit parallel interface to a Hewlett–Packard desktop computer (HP 9845B).

Probe calibration for the horizontal and vertical velocities relative to the travelling probe was achieved by rotating it in stagnant water at various tilt angles as set by the probe turntable. The background noise level was equivalent to an r.m.s. velocity of approximately 0.3 mm/s. Systematic calibration errors in the sensitivity to velocity fluctuations are estimated to be roughly 4%. Brumley (1984) gives further details on the experimental set-up and on anemometer calibration.

2.3. *Experimental procedure*

Deaerated tap water was used in the tank to prevent bubble formation owing to degassing at the hot films. After filling the tank, the surface was skimmed to reduce surface contamination by allowing sharp-crested weir-type overflow into a three-sided box pressed against the inside of the tank over an open tank port for drainage. The box was removed following this skimming procedure. To reduce the amount of dust settling on the surface after skimming, an electrostatic air cleaner was operated in the room for several hours before each experiment. When possible,

measurements nearest the surface were made first so as to have the cleanest possible surface. In spite of these precautions, it was not possible to maintain a perfectly clean surface. The implications of this are discussed below.

The procedure for taking measurements was similar to that for calibration. The sensor was brushed before each run, there was at least a three minute delay between sampling runs to allow the probe wake to decay, and the probe was reversed after sampling to avoid accumulating angular momentum. The first measurements were taken at least ten minutes after the grid was turned on to allow steady-state turbulence conditions to be approached. Each run consisted of 4095 samples of each of the data channels taken at approximately 2 mm intervals over 8 turns with the probe moving at 100 mm/s (50 Hz sampling rate). A 10 Hz low-pass second-order Butterworth filter was used in the Neff unit for each of the anemometer channels.

Spectra from preliminary trials with varying probe rotation speeds were nearly identical except for random variations and for a band centred at a wavenumber equivalent to the grid frequency. The spectral peaks often observed in this band, especially near the surface, were apparently due to grid-forced surface waves (due to flexing of the tank walls), with peak broadening due to varying angles between the wave and probe directions. In the bulk far from the surface, the grid-frequency peak was usually too small relative to the turbulence to show up. This observation, along with the Taylor frozen-turbulence criterion that the probe speed should be much larger than the r.m.s. velocity fluctuation, indicates that spectra from time series of data taken in this way can be interpreted as true spatial spectra, in spite of the fact that the probe moves at a finite speed and the velocity field near the grid depends on the phase of the grid motion. In other words, the grid behaves as a nearly ideal source to turbulence not much farther than the stroke from the grid, in that the turbulence 'forgets' the details, such as phase and mesh location, of the generating mechanism. For all the results reported here, a constant probe speed of 100 mm/s was used.

2.4. *Signal processing*

Each 4095-point data set was stored on flexible discs along with various auxiliary information such as water temperature, probe submergence and measured probe velocity to be processed at a later time. Upon being read back in, the anemometer signals were converted to horizontal and vertical velocity components using the calibration equation. Any linear trends due to spin-up or probe drift were removed by subtracting a least-square-fit straight line from each velocity component independently.

As an example, figure 2 shows the first two (of eight) turns of the time series (or 'circumferential distance series') of total horizontal and vertical velocity relative to the probe for the grid conditions of Set 3 of the varied-condition experiment at 10 mm (4 % depth) below the surface (see table 1 below). This particular data set is used in all the following example figures. The probe speed was 99.7 mm/s for this case. A small offset in each of the dashed trend lines from the nominal mean velocities (99.7 for u, 0 for w) due to probe drift can be seen, but the slight slopes in these trends are barely discernible. The probe drift was of little consequence since only the fluctuations about the trend lines were used.

Each of the resulting 4095-point velocity fluctuation records was processed by Rader's (1970) fast-Fourier-transform method to form 512-point autocovariance-function estimates with a maximum lag of 1 m (1 turn). Figure 3 shows the autocovariance-function estimates R_u and R_w for the data set that is partially

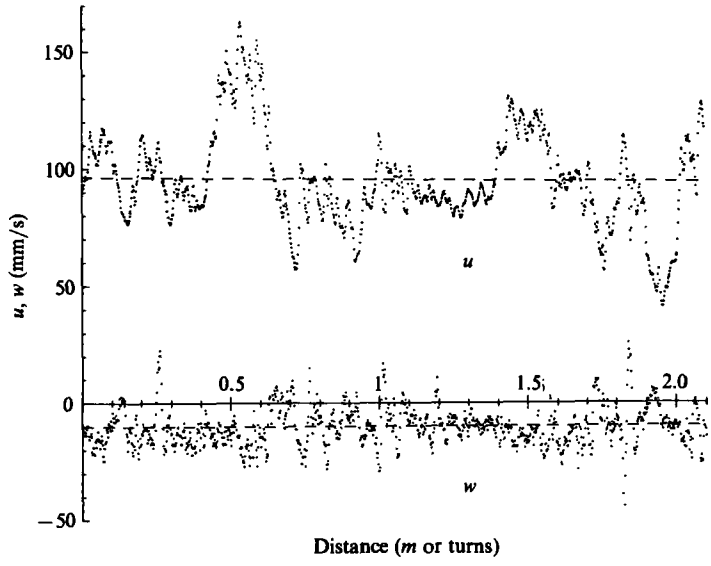

FIGURE 2. Example of total velocity time series (····) and trend lines (---); vertical velocity w bottom, horizontal velocity u top. Data shown are from the first two of eight turns at 10 mm depth for grid condition Set 3 of the varied-condition experiment.

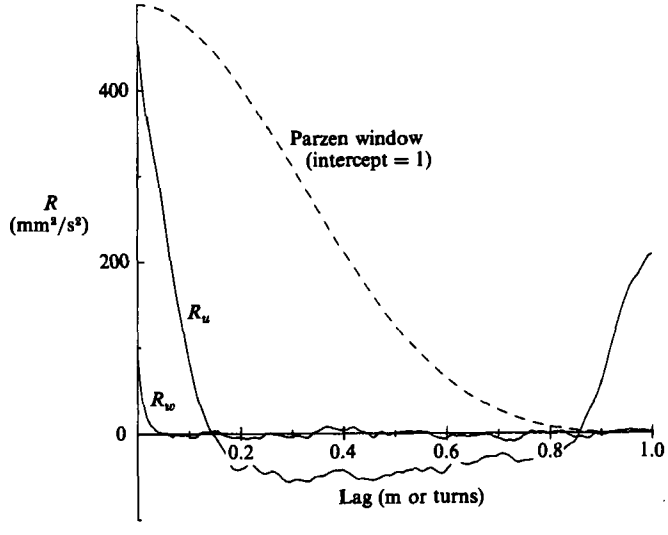

FIGURE 3. Example of autocovariance functions for vertical (R_w) and horizontal (R_u) velocity fluctuations for the data set of figure 2. The Parzen window (---) for spectral smoothing is also shown (arbitrary scale).

displayed in figure 2. The longitudinal (horizontal) autocovariance function shows a secondary peak at 1 m (that is, one turn) due to persistence of features longer than the 10 s between probe passes. Some autocovariance functions showed periodicity of shorter wavelength, causing low-wavenumber spectral peaks as discussed below.

The autocovariance-function estimates R_u and R_w were each Fourier transformed into a one-dimensional longitudinal (S_u) or transverse (S_w) power spectrum after multiplying by a Parzen (triangular convolved with triangular) window (see figure 3) with an effective width of 0.53 m. Each point of the power spectrum ideally has

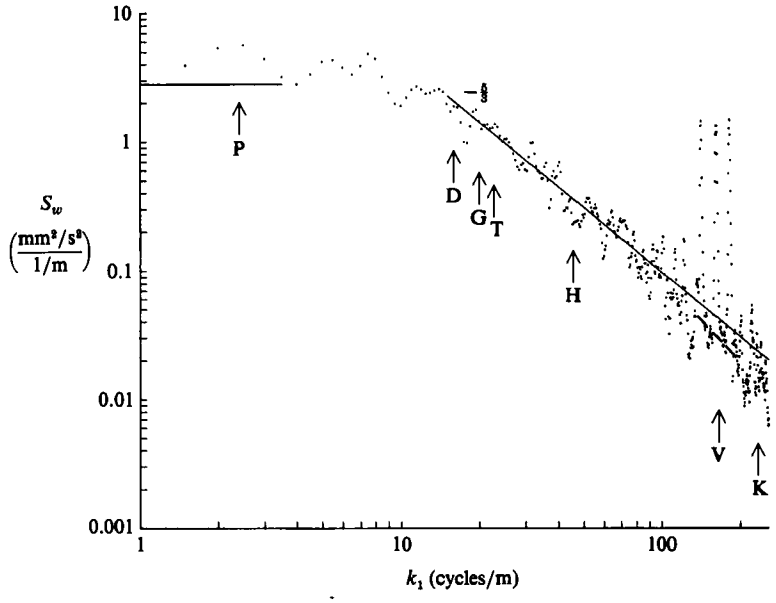

FIGURE 4. Example of transverse (vertical velocity) power spectrum for the data set of figure 2 showing manual processing. Letters indicate wavenumbers corresponding to: P, low-wavenumber peak; D, depth; G, grid frequency; T, tachometer pole frequency; H, harmonic of tachometer pole frequency; V, mechanical vibration resonances; K, Kolmogorov scale.

a chi-square distribution with (2/0.53)(4095/512) = 30 degrees of freedom. The 95% confidence interval for the spectrum of a single data set lies between 64% and 179% of the spectral estimate. The relatively wide window was used so that the tach ripple harmonics and other periodic noise components (apparently due to probe support and tower vibration modes) could be isolated as relatively narrow spikes and removed. After dividing by the transfer function of the Butterworth filter to restore the pre-filter behaviour near the filter cutoff frequency, the raw spectra were processed manually (using a cursor on the computer screen) to remove tach ripple and other noise spikes from the spectra, replacing them with a line fit to the background turbulence level at either side of the spike.

As an example the transverse power-spectrum estimate S_w (the horizontal spectrum of vertical velocity fluctuations) is shown on a log–log plot in figure 4. The set of dots is the Fourier transform of the autocovariance function R_w shown in figure 3. A $-\frac{5}{3}$ power law can be seen to fit the spectrum well between the breakpoint wavenumber $\frac{1}{2}\pi y$, indicated by D for 'Depth', and the Kolmogorov viscous cutoff, indicated by K. Three noise spikes (probably caused by mechanical vibration) are indicated by V in the figure. These were replaced by the three short 'background-estimate' lines shown. On other spectra of lower intensity, similar spikes often appeared at wavenumbers corresponding to the tach ripple and its first harmonic (indicated by T and H, respectively) and occasionally near the grid stirring frequency (indicated by G). Such spikes were removed if they contained a significant amount of kinetic energy.

At the low-wavenumber end of the spectrum, peaks were often observed at wavenumbers of 1, 2, 4 or 6 cycles per m (cycles per turn). These were probably due to large-scale grid-forced circulations that were steady, or at least persisted over periods comparable with the 80 s sampling time. Flow-visualization studies using dye

and tracer particles failed to reveal any discernible coherent or steady flow structure for the large-scale motions. Although the large-scale motions represent only a small fraction of the total kinetic energy, they do cause difficulties in defining and measuring integral lengthscales. Brown (1970), Brumfield (1977), TT and HT had similar problems with low-wavenumber components from various sources in flumes and grid-stirred tanks, and had to use somewhat artificial means to extract integral lengthscales from their data. The simpler but equally artificial method used here was to fit a horizontal line (using a cursor on the computer screen) across the base of the low-wavenumber peaks on a log–log spectral plot to extract an intercept $S_u(0)$ or $S_w(0)$. The area under the spectrum below this line (that is, not including the peak) was assumed to represent the square of the turbulent component of the velocity, u' or w'. An example of such a line truncating a peak of about 2 cycles per m is indicated by P in figure 4.

The integral lengthscales were calculated from the intercepts using the turbulent velocities as (Tennekes & Lumley 1972):

$$L_u = \frac{S_u(0)}{4u'^2}, \tag{3}$$

$$L_w = \frac{S_w(0)}{4w'^2}. \tag{4}$$

Because of the crude method of extrapolating the spectral intercepts $S_u(0)$ and $S_w(0)$, L_u and L_w can only be considered rough estimates ($\pm 50\,\%$) of the respective lengthscales. Other estimates, such as $1.8/(2\pi k_0)$, where k_0 is the wavenumber at which $kS_u(k)$ or $kS_w(k)$ is maximized, gave similar but more scattered results.

The velocity scales and lengthscales discussed above are outer scales in that they are most sensitive to the larger-scale (lower wavenumber) behaviour of the spectra. The behaviour of each spectrum in the inertial subrange can be described as a straight line with slope $-\frac{5}{3}$ on a log–log plot) and with a magnitude at fixed wavenumber ideally proportional to the $\frac{2}{3}$ power of the dissipation rate. Such a line has been fitted manually in figure 4. Using the relations for isotropic turbulence (Tennekes & Lumley 1972), each spectrum can be used to define a parameter ϵ_u or ϵ_w, called the 'dissipation rate' here for convenience, but not actually a direct measure of the true dissipation rate, as

$$\epsilon_u = 2\pi c^{-\frac{3}{2}}(\tfrac{55}{9})^{\frac{3}{2}}[\langle k_1^{\frac{5}{3}} S_u \rangle]^{\frac{3}{2}}, \tag{5}$$

$$\epsilon_w = 2\pi c^{-\frac{3}{2}}(\tfrac{55}{12})^{\frac{3}{2}}[\langle k_1^{\frac{5}{3}} S_w \rangle]^{\frac{3}{2}}, \tag{6}$$

where it is assumed that $c = 3.0$, and $\langle\ \rangle$ represents an average over a range of wavenumbers in the inertial subrange.

2.5. *Experimental programme*

The results of two turbulence-measurement experiments are presented in this paper. One, called the 'detailed-profile experiment', involved measurements at many stations at varying distances below the surface under a single set of grid conditions. In the other, called the 'varied-condition experiment', profiles were taken at only four stations for each of several combinations of grid parameters and water depths.

For the detailed-profile experiment, twenty data sets were recorded at 13 stations between 0.4 and 167 mm depth (0.16 and 67 % of the grid depth z_s). Of these, two were checks of background noise, probe wake and residual motion when the grid was turned off, and five were repeated measurements at 3 and 60 mm (1.2 and 24 %) depth

Grid condition Set	Nominal f (Hz)	Stroke S (mm)	z_s (mm)	Temperature (°C)	$u_{HT}z$ (mm²/s)	R_λ
1	1.15	99	248	21.6	2260	84
2	1.63	99	248	22.2	3200	100
3	1.97	99	248	23.3	3870	112
4	1.28	48	248	23.2	850	52
5†	2.56	48	249	24.0	1700	74
6	3.79	21.6	248	23.2	760	49
7	1.66	21.6	248	22.9	330	33
8	2.95	21.6	165	22.8	590	43
9	1.63	21.6	165	22.8	330	32
10	3.19	48	164	22.8	2110	82
11	1.70	48	164	22.9	1130	60
12	1.96	99	164	22.9	3850	111

† Grid conditions of the detailed-profile experiment.

TABLE 1. Grid conditions for the varied-condition experiment

to indicate repeatability. The conditions were identical with one of the cases (Set 5, see table 1) of the varied-condition experiment: grid frequency nominally 2.56 Hz, stroke 48 mm and cover (depth of top of grid at top of stroke) 211 mm. Assuming a virtual origin at the centre of the grid stroke, coinciding approximately with that measured by TT and HT, the surface distance (or average grid depth) z_s is simply the cover plus half the stoke plus one bar thickness, or 249 mm in this case. In both experiments, the virtual origin was always 144 mm above the bottom of the tank.

For varied-condition experiment, data sets were collected only at 3, 10, 30, and 60 mm in those cases when the grid depth z_s was approximately 250 mm and at 2, 7, 20, and 40 mm when z_s was two-thirds as deep, or approximately 167 mm. Hence in all cases, the depth stations were at 1.2, 4, 12, and 24 % of z_s. For each of the two grid depths z_s, four-point profiles were taken at each of three strokes, nominally 1, 2, and 4 in. (actually 21.6, 48, and 99 mm), at an assortment of grid frequencies, for a total of 12 four-point profiles taken over two experimental days four days apart. The 12 sets of grid conditions are listed in table 1. Also listed are the grid action, as parametrized by $u_{HT}z$ (from (2)) and R_λ, a measure of the turbulent timescale ratio (estimated from the grid parameters as $R_\lambda = [15u_{HT}(2az)/\nu A]^{\frac{1}{2}}$, with $a = 0.1$ and $A = 1$).

2.6. *Normalization of experimental results*

The varied-condition experiment covered a range of grid depths z_s and grid actions $u_{HT}z$ resulting in a wide range in the magnitudes of the velocity and dissipation measurements. In order to compare the results from the different conditions, it is convenient to normalize each profile by some scale factor representing its overall magnitude. This procedure allows the shapes of the profiles to be directly compared with each other and with theoretical shapes, and also provides, via the scale factor, a simple means of comparing the magnitudes of the measurements under different conditions. Because of the considerable scatter in the data, the simplest normalization technique, using the deepest (24 %) measurement as the scale factor for each set of conditions, gave unsatisfactory results, so the least-squares technique described below was used instead.

For consistency, the same procedure was applied to all six turbulent quantities:

the r.m.s. turbulent velocity fluctuations u' and w', the integral lengthscales L_u and L_w and the dissipation-rate estimates ϵ_u and ϵ_w. (It was not necessary to normalize the integral-lengthscale profiles with anything other than the grid depth z_s, but the least-squares normalization provided a convenient averaging technique.) To interpret the results of the varied-condition experiment, each profile was assumed to represent the product of a universal normalized profile factor f_x and a scale factor g_x for any turbulent quantity x, including a normalized error e. Using the horizontal r.m.s. turbulent velocity u' as an example,

$$u' = \left[f_u\left(\frac{y}{z_s}\right) + e\right] g_u(z_s, f, S), \tag{7}$$

where y is the distance below the surface and z_s is the distance between the surface and the virtual origin as defined above. The scale g_x (here g_u) depends on the grid conditions as represented by z_s, the grid frequency f, and the peak-to-peak grid stroke S. To fit an estimated profile f_x and set of scales g_x, any multiple data sets were averaged and then the resulting 48 data points (4 points per profile under 12 conditions) were used to make least-squares estimates to the four values of f_x and the twelve values of $1/g_x$ using (7) (linearized by dividing by g_x) along with the arbitrary normalizing assumption that $f_x(24\,\%) = 1$.

Implicit in this separation-of-factors approach is the assumption that the scale depth of the profiles (the integral lengthscale) is proportional to the grid depth z_s so that the four measurements in each profile correspond to the same relative position for every set of conditions. That this assumption is valid is verified by the integral-lengthscale measurements discussed below.

3. Experimental results

3.1. *Vertical profiles of turbulent quantities*

As described above, each set of velocity records from a measurement at a certain depth was converted to a power spectrum from which turbulent velocity, lengthscale and dissipation-rate values were extracted. Under a single set of grid conditions, such as those of the detailed-profile experiment (Set 5 in table 1), a plot of any one of these turbulent quantities versus depth forms a profile that can be compared to theoretical curves. Such profiles are systematically presented in this section for each turbulent quantity. There follows in each case a similar figure to which the normalized profiles from other grid conditions (measured in the varied-condition experiment) and their mean shape have been added. The scale factors used to accomplish the normalization are presented in §3.2, as this section is devoted to profile shape, not magnitude.

3.1.1. *Vertical velocity profile*

The profile of r.m.s. vertical velocity fluctuations w' from the detailed-profile experiment is shown in figure 5. The depth scale is normalized by $z_s = 249$ mm to be 0 at the surface and 1 at HT's 'virtual origin' (the centre of the grid stroke). The dot-dashed hyperbola (HT relation, (2)) appears to have the correct shape (i.e. proportional to $1/z$) but is roughly 20 % too large in magnitude.

The surface reduces the vertical velocity fluctuations below the bulk curve in a 'surface-influenced layer' with a relative depth of roughly 10 or 20 %, depending on how one chooses to define it. The dashed curve that follows the data in this layer

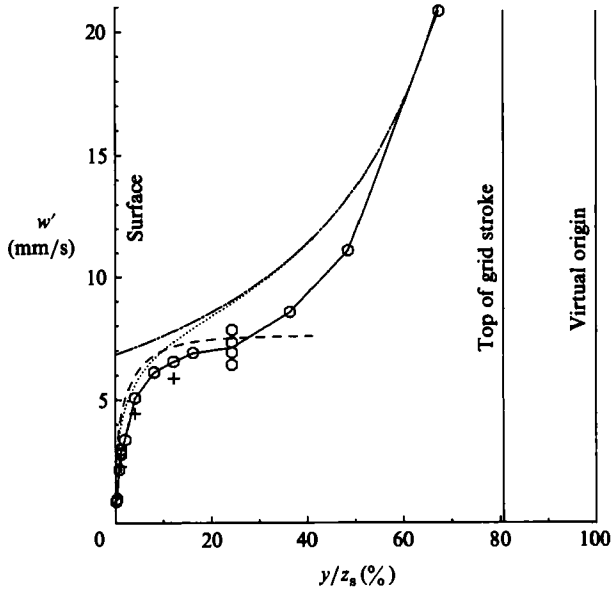

FIGURE 5. Vertical velocity-fluctuation (r.m.s.) profile plotted with a linear depth scale. ○, detailed-profile experiment; +, Set 5 of the varied-condition experiment (same grid conditions on a different day); –·–·–, HT relation; ---, HG profile; ····, combined profile.

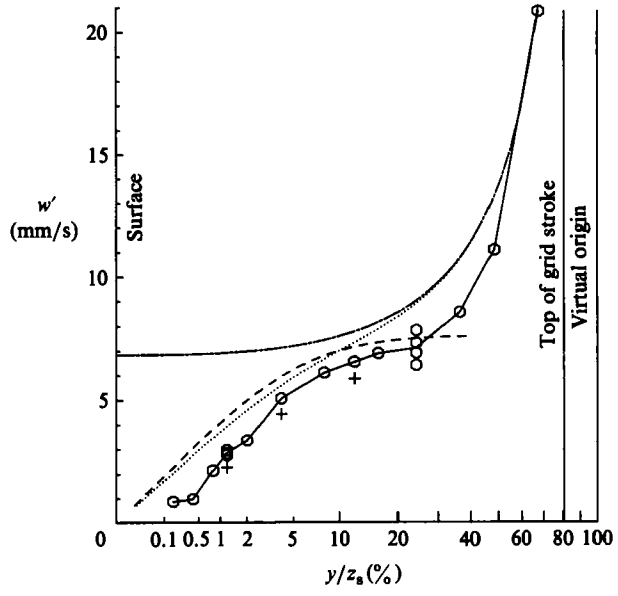

FIGURE 6. Vertical velocity-fluctuation profile. Identical with figure 5 but plotted on a depth scale with a cube-root distortion.

represents the numerical fit to the HG profile $w'(Y, w'_\infty)$ given by (A 4) in the Appendix. Y is the depth y normalized by the longitudinal integral scale L_∞ far from the surface, which is assumed here to be $0.1z_s$ (TT, see (1)). Hence $Y = 1$ at $y/z_s = 10\%$. The value used for the far-field vertical velocity fluctuation w'_∞ was calculated from the HT relation (2) with $z = 0.9z_s$; that is, the bulk velocity scale

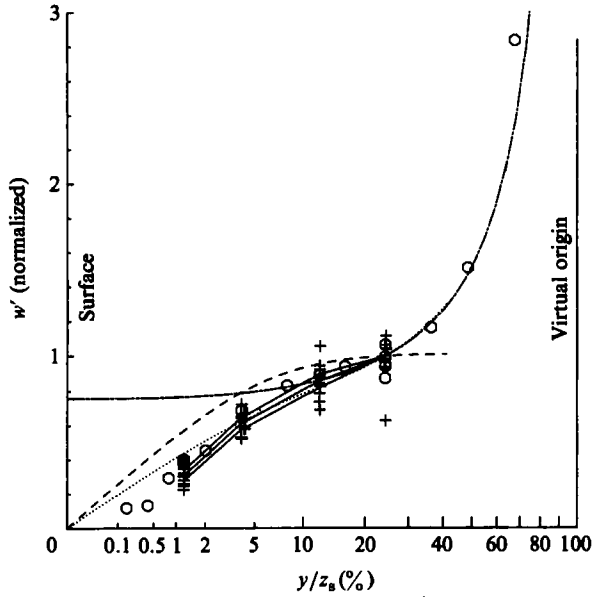

FIGURE 7. Normalized vertical velocity-fluctuation profile. +, varied-condition experiment, all sets; ——, mean and $\pm\sigma$ confidence interval for the least-squares-fitted profile factor f; other symbols as on figure 5.

one longitudinal integral lengthscale from the surface. Thus w'_∞ for the evaluation of the HG profile is a certain constant (7.6 mm/s) for the conditions of the detailed-profile experiment. The data show that the surface-influenced layer corresponds to HG's theoretical 'source layer'. The dotted curve in figure 5 is a combination of the HT and HG profiles just described. Like the dashed curve, it is also generated using (A 4), except that w'_∞ is calculated from (2) at the local grid distance $z = z_s - y$ rather than the fixed distance $0.9z_s$.

These three curves have identical or analogous meanings for all of the profile figures below. Note that no parameters have been adjusted to fit any of these profiles to the data of these experiments.

Because the surface-influenced layer is of primary interest but only occupies 10 or 20% of the depth, it is convenient to plot the data on a distorted depth axis, as in figure 6, which is otherwise identical with figure 5. A cube-root distortion is appropriate because this makes the HG profile appear asymptotically linear at small depths, and also because one longitudinal integral lengthscale occurs near the centre of the figure ($0.1\frac{1}{2} = 46\%$ relative depth). Again, a roughly 20% difference in magnitude is apparent between the data and the literature-derived curves.

The same detailed-profile experiment data are again shown in figure 7, but now with the profiles from the varied-condition experiment added. This time the profile has been normalized so as to average 1 at 60 mm (relative depth 24%), which corresponds to the deepest level of the varied-condition experiment. The same three literature curves as before are also plotted so as to be normalized to 1 at this point. The four measurements of each profile of the varied-condition experiment have been normalized by the scale factor $g_{w'}$ for that set of grid conditions as determined by least-squares fit (see §2.6). The solid line passing through the varied-condition data connects the four average profile points $f_{w'}$, determined by the least-squares fit. The lines above and below the average profile represent a 68% confidence interval (i.e.

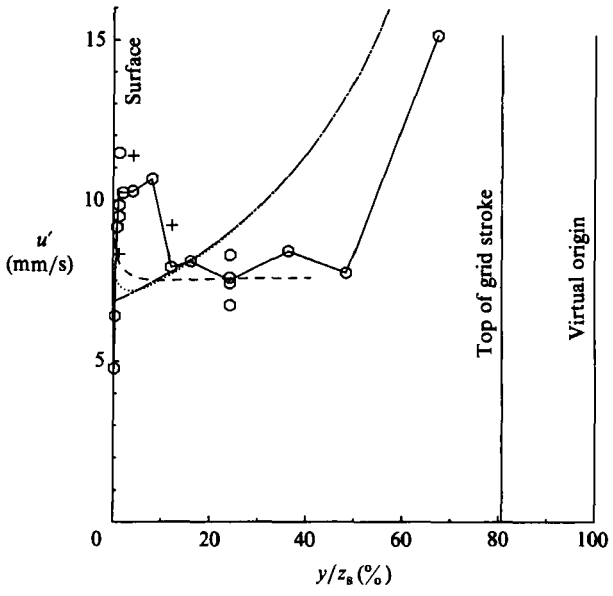

FIGURE 8. Horizontal velocity-fluctuation profile (linear depth scale). Symbols as on figure 5.

plus or minus one standard deviation) for the estimated average profile. The confidence interval has zero width at 24 % relative depth because the average profile is forced to have a value of 1 there.

The presentation of the results in normalized form in figure 7 shows that when the considerable scatter in the varied-condition profiles is averaged out and when scale differences are eliminated by normalization, the profile shape in the bulk and in most of the surface-influenced layer agrees well with the combined HG/HT profile represented by the dotted line. The varied-condition measurements at the shallowest (1.2 %) relative depth and the detailed-profile measurements at the three shallowest (0.16, 0.4, and 0.8 %) relative depth fall significantly below this curve, however. The data are consistent with the existence of a viscous boundary layer. According to Hunt (1984*a*), the thickness of the viscous boundary layer would be expected to be of the order of $L_\infty R_L^{\frac{1}{2}}$, the longitudinal integral lengthscale divided by the square root of the turbulent Reynolds number. The turbulent Reynolds number varies with the grid conditions, of course, but the value of about 400 for the detailed-profile experiment is typical. For that case, the viscous-layer thickness would be expected to be roughly 5 % of the integral lengthscale, or roughly 0.5 % relative depth. Hence, the observed boundary layer appears to have a thickness of the right order of magnitude to be interpreted as a viscous boundary layer.

3.1.2. *Horizontal velocity profile*

The horizontal velocity-fluctuation measurements (figures 8 and 9) from the detailed-profile experiment fall substantially below the HT relation throughout the bulk of the tank, but form a 'bulge' in the surface-influenced layer above all the literature curves. The three measurements marked by + at 1.2, 4 and 12 % relative depth taken under the same grid conditions during the varied-condition experiment on a different day show that this bulge is a repeatable phenomenon. Bulges in the surface-influenced layer occur at some of the other grid conditions in the varied-condition data, but the profile with the particular conditions of the detailed-profile

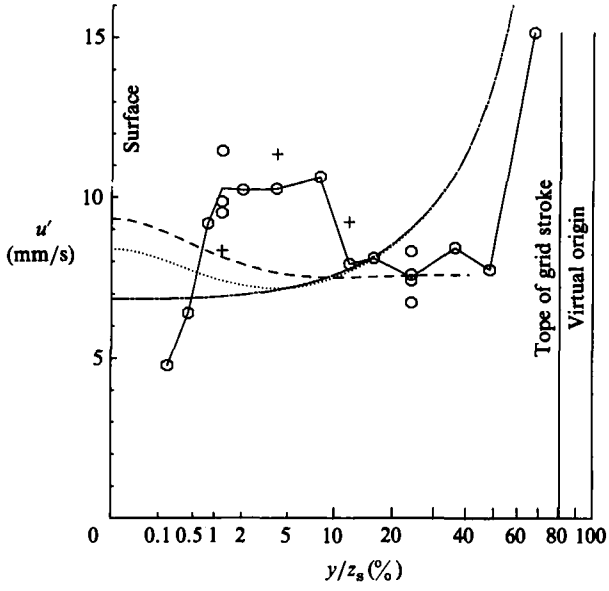

FIGURE 9. Horizontal velocity-fluctuation profile (cube-root depth scale). Symbols as on figure 5.

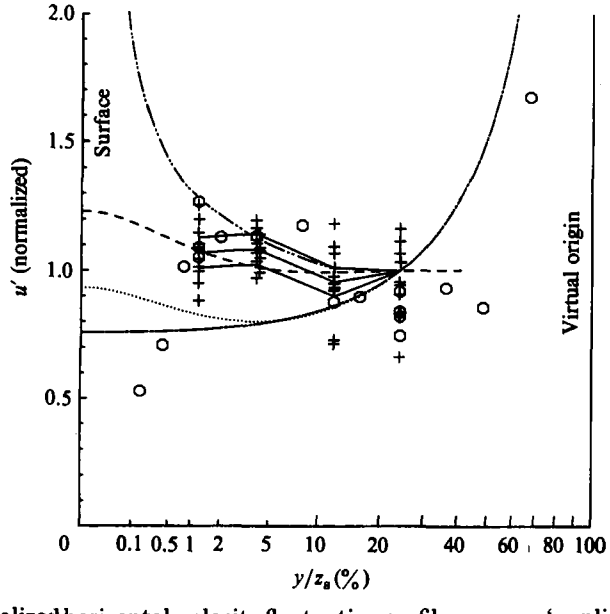

FIGURE 10. Normalized horizontal-velocity fluctuation profiles. —··—, 'nonlinear correction' profile, equation 2.20*b* of Hunt (1984*b*). Symbols as on figure 7.

experiment happens to have the greatest bulge, even though the conditions were moderate with respect to the experimental ranges of the grid parameters.

The surprising deviations of the horizontal velocity fluctuations from a reasonable profile in both the bulk and in the surface-influenced layer may be attributed to the fact that the average fluctuations along the probe path may not be a representative sample of the conditions throughout the tank at a particular depth. McDougall's

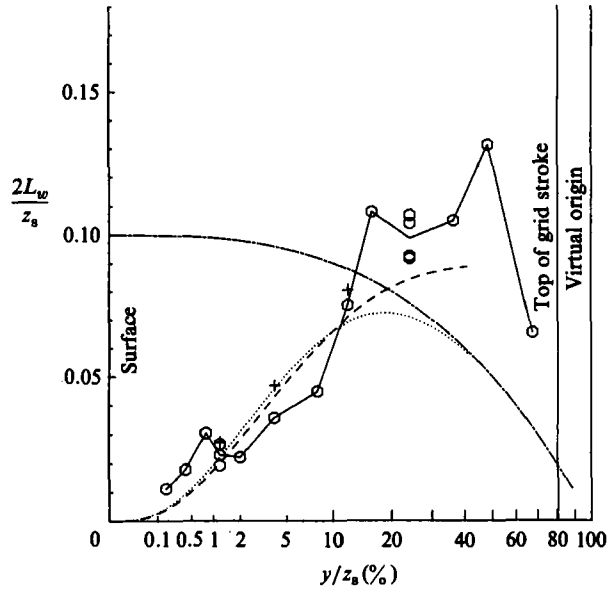

FIGURE 11. Transverse integral-lengthscale profile, shown doubled (cube-root depth scale). —·—·, TT relation; ——, HG profile; ····, combined profile; other symbols as on figure 5.

(1979) measurements indicate thet substantial non-uniformity in horizontal velocity fluctuations may occur. The large patternless scatter in the horizontal velocity-fluctuation profiles from the varied-condition experiment (figure 10) is probably also due to this problem.

Normalized horizontal-velocity profiles are shown in figure 10. A slight bulge seems to remain in the averaged profile, but the shape is not significantly different from that of the dashed HG curve (with constant u'_∞).

Evidence for a viscous boundary layer is also seen in the horizontal velocity-fluctuation profile (figure 10). As in the vertical velocity-fluctuation profile (figure 7), a boundary-layer effect is seen in the three shallowest values of the detailed-profile experiment. Although an extrapolation to the surface cannot be made with confidence, it is apparent that there is a substantial reduction in the horizontal velocity fluctuations at the surface.

Also plotted is the 'nonlinear correction' profile of Hunt (1984*b*) that is supposed to estimate the amplification effect on horizontal velocity fluctuations due to vortex stretching in fluctuating stagnation flow induced by the larger eddies. The measurements are consistent with this profile outside of the viscous boundary layer, which obscures the most interesting part of the profile at the range of Reynolds numbers of these experiments. But they are not sufficiently accurate to determine whether the fit is better than that of the original HG profile.

3.1.3. *Transverse integral-lengthscale profile*

The transverse integral lengthscale L_w (that is, the horizontal correlation length along the circular probe path of vertical velocity fluctuations) was estimated from the extrapolated intercept of the vertical velocity spectrum (see §2.4). Figure 11 shows the doubled lengthscale profile for the detailed-profile experiment as normalized by the depth $z_s = 249$ mm of the grid virtual origin versus the cube-root distorted depth scale. The dot-dashed line proportional to the distance from the grid

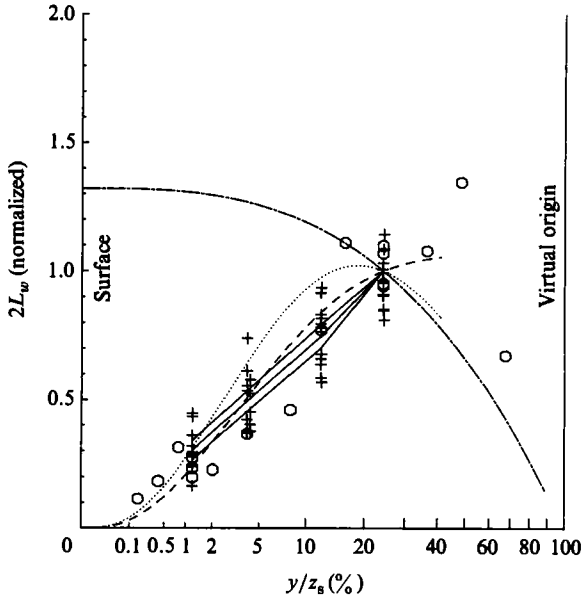

FIGURE 12. Normalized transverse integral-lengthscale profile. Symbols as on figure 11.

origin ((1) with $a = 0.1$) is the result of TT for the longitudinal integral scale L_u in the bulk. For isotropic turbulence, this should be the same as $2L_w$ (Tennekes & Lumley 1972). The other two curves are given by the numerical approximation to the HG transverse integral-scale profile (A 6). In a manner entirely analogous to the method of calculating the w' and u' profiles above, the dashed HG profile is calculated using a fixed value of L_∞ from the TT relation (1) at 10% relative depth ($L_\infty = 0.1$ $(0.9z_s) = 22.4$ mm) while the dotted combined curve is calculated using the TT value for L_∞ at the local grid distance ($L_\infty = 0.1z = 0.1$ $(z_s - y)$).

The TT line seems to underestimate $2L_w$ in the bulk. HT also found this to be the case for the longitudinal integral scale L_u as discussed in §1. Comparison of figure 11 with figure 9 reveals a close correlation between the deviations in the L_u and u' data from a smooth curve, suggesting that they stem from the same cause, possibly the effect horizontal non-uniformity as observed by McDougall (1979). In the surface-influenced layer, the strong reduction in the transverse integral scale L_w due to the presence of the surface is clearly evident.

In figure 12, the normalized transverse integral-scale data from both the detailed-profile and varied-condition experiments and normalized literature curves and plotted in the same manner as the velocity fluctuations above. The varied-condition profiles show that the downward bulge in the detailed profile between 2 and 8% relative depth is not typical.

3.1.4. *Longitudinal integral-lengthscale profile*

The longitudinal integral scale L_u (that is, the horizontal correlation length of horizontal velocity fluctuations along the probe path) was estimated from the extrapolated intercept of the horizontal velocity spectrum (figure 13). The dot-dashed TT line (1) is the same as above, but the HG and combined profiles are now given by (A 7).

As with the doubled transverse integral scale $2L_w$, the longitudinal integral scale L_u seems to be underestimated in the bulk by the TT line. The longitudinal integral

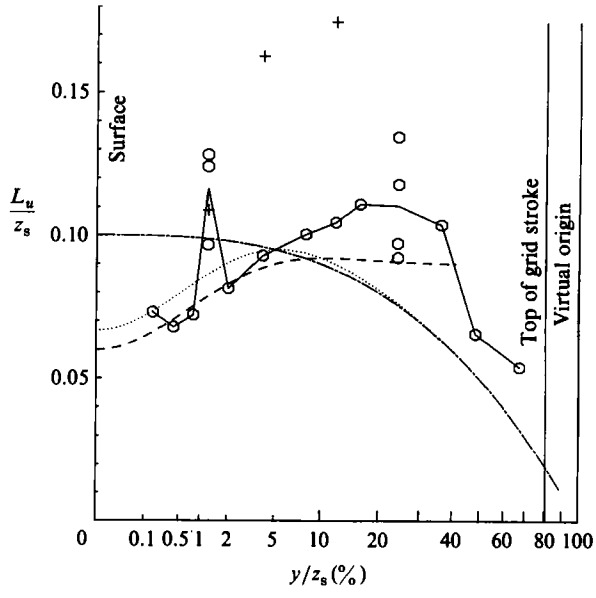

FIGURE 13. Longitudinal integral-lengthscale profile. Symbols as on figure 11.

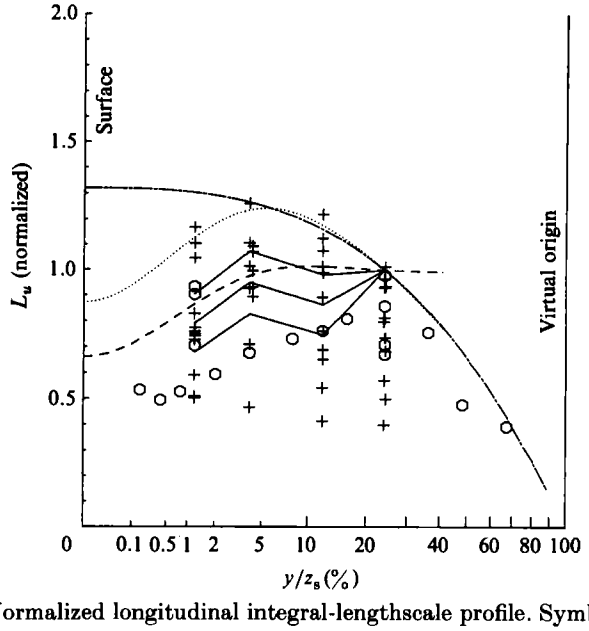

FIGURE 14. Normalized longitudinal integral-lengthscale profile. Symbols as on figure 11.

scale is theoretically reduced by one-third at the surface, and this surface effect is clearly shown in the detailed profile.

The normalized profiles from the detailed-profile and varied-condition experiments are shown in figure 14 in the same manner as before. A large amount of scatter in the data is evident. The mean profile (f_{L_u}) suggests some surface effect, as predicted by the dashed HG curve, although plots of individual profiles showed no consistent pattern.

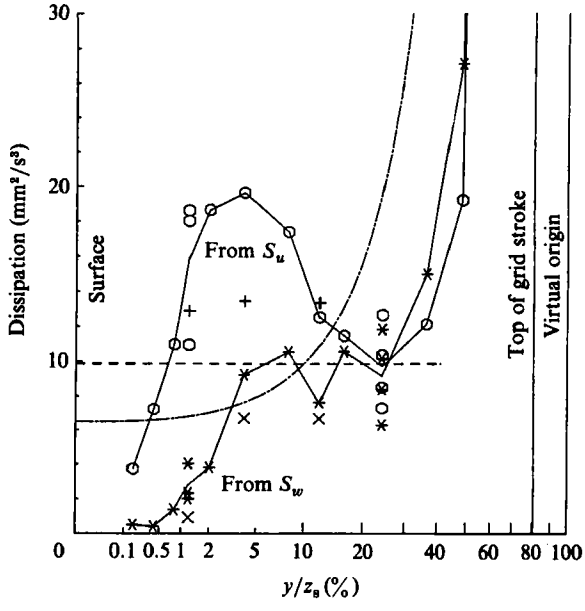

FIGURE 15. Dissipation-rate profile. —·—·, z^{-4} decay; ---, constant dissipation rate; *, ×, ϵ_w estimates; ○, +, ϵ_w estimates; ○, *, from detailed-profile experiment; +, ×, from Set 5 of the varied-condition experiment.

3.1.5. *Dissipation-rate profile*

The symbols ϵ_u and ϵ_w are used here for dissipation-rate estimates indicating the magnitudes of the horizontal and vertical velocity spectra S_w and S_u, respectively, in the inertial subrange (see §2.4). Dissipation-rate profiles for ϵ_u and ϵ_w are plotted for the detailed-profile experiment (along with the data at the three depths of Set 5 of the varied-condition experiment) on a cube-root depth scale in figure 15. Also shown is a dot-dashed curve proportional to z_s^{-4} (where $z = z - y$ is the distance from the grid origin) that represents the estimate $\epsilon = u'^3/(2L_u)$ (Tennekes & Lumley 1972), where the HT $u_{HT}(z)$ relation (2) is used for u' and the TT relation (1) is used for L_u. This is the expected profile in the bulk of the fluid far from the surface. The other dashed line represents a constant dissipation rate (as in the HG theory) equal to the above estimate at 10% relative depth.

The data at the lowest point (67% relative depth) are off scale in figure 15 but lie well below the z^{-4} curve. Likewise, all of the estimates in the bulk lie well below this curve, and in fact lie closer to the constant-dissipation-rate line throughout the upper half of the tank. Clearly, if the turbulence in the tank were horizontally homogeneous, the dissipation rate would have to decay with distance from the grid, and so cannot be constant in the bulk. Therefore, the dissipation data in the detailed-profile experiment suffer from the same horizontal non-homogeneity problem seen above in the u' and L_w profiles. This shows that the problem is not simply an artifact of the data processing to remove the large-scale mean motions, but affects the inertial subrange of the spectra as well.

The dissipation-rate estimates from the two kinds of spectra S_u and S_w agree well in the bulk where the turbulence is not far from being isotropic, but the estimate ϵ_u is greater than ϵ_w in the surface-influenced layer where anisotropy seems to affect the inertial subrange in spite of the theoretical principle that the smaller scales of the turbulence should be isotropic. The dissipation-rate estimates closest to the

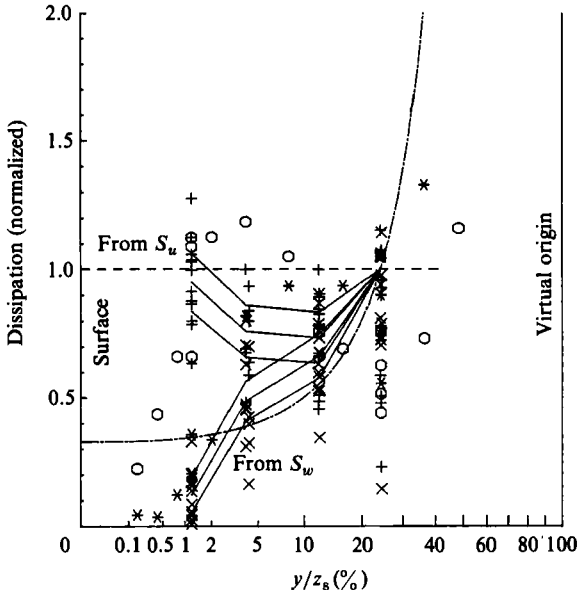

FIGURE 16. Normalized dissipation-rate profiles. The symbols are the same as in figure 15 except +, ×, which are from all sets of the varied-condition experiment.

surface that suggest a viscous sublayer are probably invalid because a true inertial subrange does not exist for the spectra from which they were derived.

Figure 16 shows the normalized ϵ_u and ϵ_w profiles from both the detailed-profile and varied-condition experiments. The mean profiles (f_{ϵ_u} and f_{ϵ_w}) and 68% confidence intervals for ϵ_u (upper profile) and ϵ_w (lower profile) from the varied-condition least-squares fit are also shown. As with the other profiles, the bulge of the detailed profile in the surface-influenced region is not typical. The mean ϵ_u profile, in fact, seems to have a minimum value near 10% relative depth (one integral lengthscale from the surface according to (2) and then increases towards the surface. The mean ϵ_w profile, on the other hand, closely follows the expected z^{-4} decay curve.

3.2. *Scale factors*

As shown by (7), each of the profiles from the varied-condition experiment was separated by least-squares fit into the product of a normalized mean profile, discussed in §3.1, and a scale factor depending on the grid conditions, discussed here. Being independent of depth, a scale factor acts as a functional of the profile, summarizing in a single number the magnitude of the particular turbulent parameter in the near-surface environment, and thus providing a useful measurable variable characterizing the turbulence. The scale factor used here is simply the value the profile would have at a certain arbitrary relative depth (chosen as the depth of the deepest measurement, 24%) if the measured profile had the shape of the mean profile (that is, variations about the mean profile are averaged out by the fitting procedure).

Following Long's (1978) argument that grid-generated turbulence some distance from the grid source can be characterized by a single combination of grid parameters (the grid 'action'), we choose to characterize the action by a bulk Reynolds number $R_L = u_{\mathrm{HT}}(2az)/\nu$, with $a = 0.1$ (1). This Reynolds number is independent of depth because of the z^{-1} dependence of the HT velocity, and so depends only on the grid parameters, of which only the grid frequency and stroke vary in the varied-condition

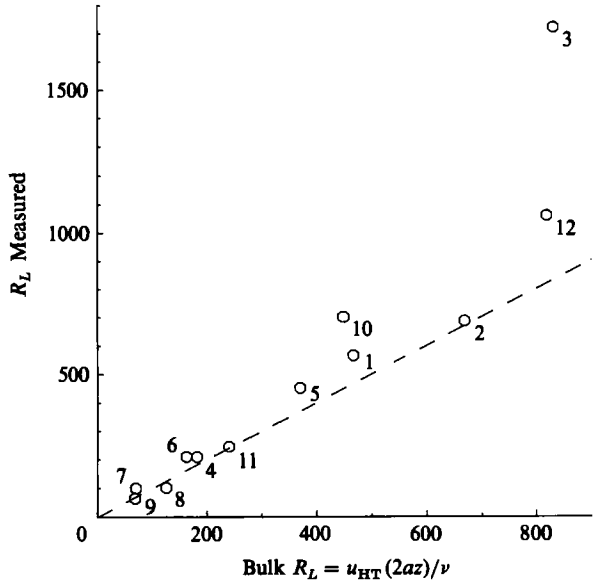

FIGURE 17. Measured turbulent-Reynolds-number estimate $R_L = [\frac{1}{3}g_w^2 + \frac{2}{3}g_u^2]^{\frac{1}{2}} 2g_{2L_w}/\nu$ versus bulk turbulent Reynolds number from grid parameters (equations (1), (2)), with $a = 0.1$; ---, line of slope one.

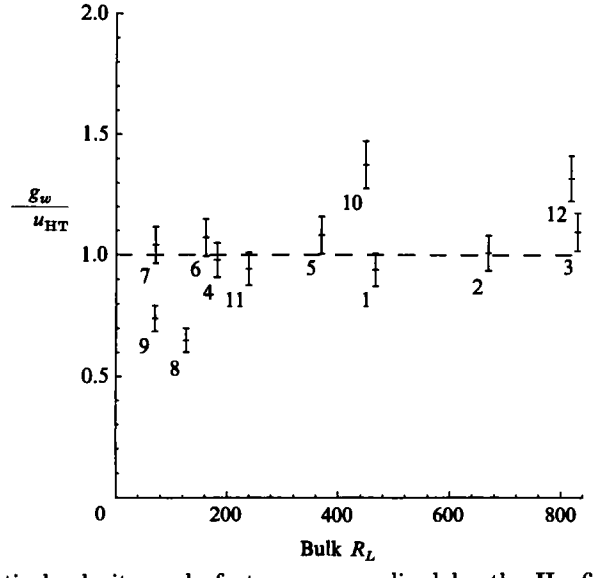

FIGURE 18. Vertical-velocity scale factor g_w normalized by the Hopfinger–Toly velocity u_{HT}, plotted as a function of bulk Reynolds number $R_L = u_{HT}(2az)/\nu$. Numerals signify grid condition set from table 1. Error bars show $\pm$ one standard deviation of the estimate of the scale factor.

experiment. Hence, any deviations of the measured scale factors from the predictions of the HT relation for the velocity scales or the TT relation for the integral lengthscales (due to near-surface viscous effects, for instance) should be functions of the bulk Reynolds number, R_L.

Before examining plots of the scale factors as functions of the grid Reynolds number, it is of interest to ask to what degree the bulk R_L is a good estimate of

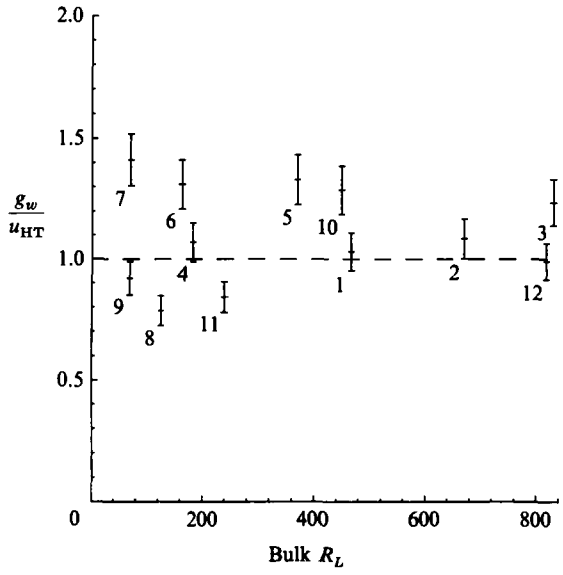

FIGURE 19. Horizontal-velocity scale factor g_u normalized by u_{HT} plotted as a function of grid Reynolds number. Symbols as on figure 18.

a turbulent Reynolds number derived from measurements. Such a comparison is made in figure 17. The vertical axis is the measured turbulent Reynolds number defined as:

$$R_L = \frac{[\frac{1}{3}(2g_u^2 + g_w^2)]^{\frac{1}{2}}[2g_{2L_w}]}{\nu} \tag{8}$$

where g_u, g_w and g_{2L_w} are the scale factors for u', w' and $2L_w$, respectively. This is a convenient and straightforward estimate from the measurements of the Reynolds number that would have occurred in the vicinity of the surface were the surface not present. The scale factor of the transverse integral scale was used rather than that of the longitudinal lengthscale because of the lower scatter in the data. With the exception of one point (Set 3) which had problems with the integral-lengthscale measurements, there is reasonable agreement considering the scatter in the measurements, although the measured Reynolds numbers seem to average some 15 % higher than the bulk estimates from grid parameters.

The normalized scale factors g_w/u_{HT} and g_u/u_{HT} for the vertical and horizontal velocity fluctuations are plotted against bulk R_L in figures 18 and 19, respectively. The scale factors have been normalized by the HT velocity scale at the surface (that is, using (2) with $z = z_s$). The bars represent plus or minus one standard deviation about the fitted value at the centre of each symbol, as estimated from the least-squares fit. The number beside each symbol indicates the set of grid conditions (table 1). There does not appear to be any significant overall trend in these velocity scale factors with Reynolds number.

The average value of g_u/u_{HT} over the twelve date sets is 1.11 compared to the literature-derived value of 1.32 (using g_u calculated from the combined HT/HG profile at 24 % depth). The average value of g_w/u_{HT} is 1.02. The average anisotropy g_w/g_u of 0.93 was not significantly different from 1, but was significantly less than the values of 1.1–1.4 found in other grid experiments. These results indicate that the HT velocity calculated at the surface is a reasonable (within 20 %) turbulent-

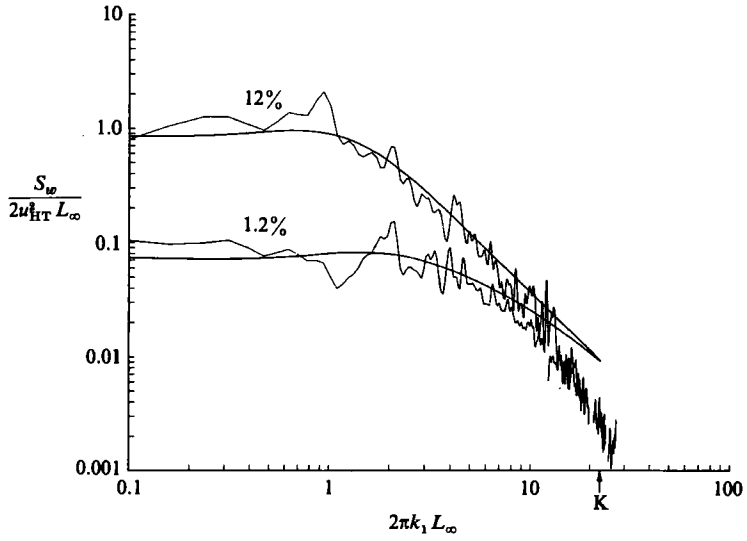

FIGURE 20. Transverse power spectra of vertical velocity at 12% depth (upper) and 1.2% depth (lower) (120 and 12% of L_∞, respectively) from the detailed-profile experiment. Both spectra are normalized by the spectral intercept $S_w(0) = 2u_{HT}\,2L_\infty$ and breakpoint $\frac{1}{2}\pi L_\infty$ that would be expected at the surface were the surface not present. ——, Spectra predicted by the HG source theory.

velocity-scale estimate for interfacial transfer studies in grid-stirred tanks where turbulence data is lacking. Brumley (1984) gives the additional scale factors for lengthscales and dissipation rates (not presented here). In summary, the data behave similarly to the velocity scale factors given above and, on the whole, confirm that all scale factors are independent of R_L.

3.3. *Spectra*

Two transverse spectra of vertical velocity (at 1.2 and 12% relative depth) are compared with the HG theoretical spectra in figure 20. The axes are normalized by the constants $2u_{HT}^2 L_\infty = 2.3$ m mm^2/s^2 and $(2\pi L_\infty)^{-1} = 6.4$ cycles per m, respectively, which are evaluated at the surface using (1) and (2). Thus the ordinate value 1 on figure 20 represents the intercept $S_w(0)$ (equation (4)) and the abscissa value 1 represents the breakpoint wavenumber that the spectrum would theoretically have at a distance z_s from the grid were the surface not present (i.e. for isotropic turbulence).

The HG theoretical spectra have been adjusted to the local scales in the manner of the combined HT/HG profiles above. The agreement in both slope and magnitude between the measured and theoretical spectra is remarkable in the light of the fact that no parameters have been fitted. The HG theory does not attempt to properly predict the spectra in the vicinity of the Kolmogorov cutoff, denoted by K in figure 20. The spectrum at 12% relative depth, or roughly one integral lengthscale L_∞ from the surface, shows little surface effect, whereas the spectrum ten times closer to the surface is suppressed at low wavenumbers because eddies larger than the depth are constrained by the surface. Hence the breakpoint between the flat and $-\frac{5}{3}$ slope portions of the spectrum occurs at a dimensionless wavenumber L_∞/y corresponding to the depth, which is ten times higher for the shallower spectrum.

More selected vertical velocity spectra from the detailed-profile experiment are

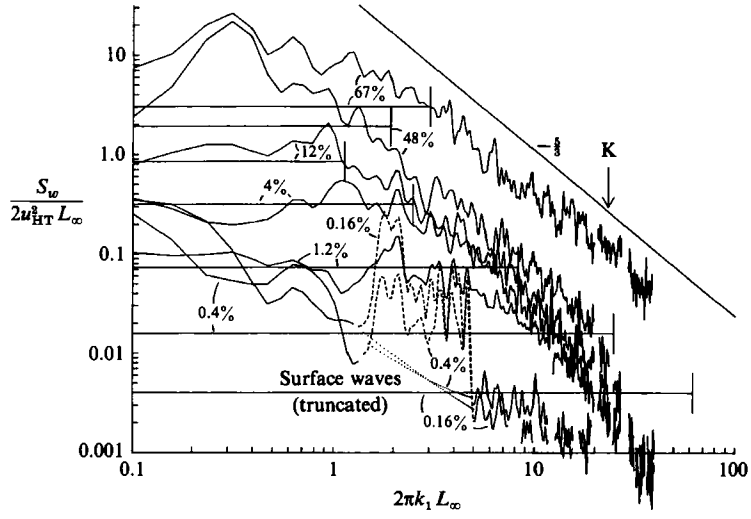

FIGURE 21. Transverse power spectra of vertical velocity at selected depths from the detailed-profile experiment. Normalization as in figure 20. Depths labelled as a percentage of grid-to-surface distance z_s. Horizontal bars are predicted spectral intercepts, vertical marks at right ends are predicted breakpoints based on the HG theory with local HT and TT scaling. K, Kolmogorov cutoff.

plotted in figure 21 on the same axes as figure 20. As a guide for comparison, the HG prediction corresponding to each measured spectrum is shown in schematic form as a bar at a level corresponding to the $k_1 = 0$ intercept and ending in a hash mark at the breakpoint. These predictions have been adjusted using (1) and (2) to account for the scaling of the local values of u_{HT} and L_∞ with distance from the grid.

From bottom to top of figure 21, the spectra were taken at depths progressively farther from the surface. The relative depth y/z_s is labelled for each curve. The two highest spectra from the bulk (48 and 67 %) show the decay on all scales that occurs with increasing distance from the grid. The three central spectra from the surface-influenced layer (1.2, 4, and 12 %) tend to fall on top of each other at the higher wavenumbers, showing a relatively constant dissipation rate throughout this layer (compare with figure 15). The suppression by the surface of the spectra at wavenumbers below the breakpoint as seen in figure 20 is further evident here for depths in the surface-influenced layer.

The turbulent Reynolds number was high enough ($R_L = 390$, $R_\lambda = 74$) for an inertial subrange following a $-\frac{5}{3}$ power law to exist. The surface suppression effect of course affects the low-wavenumber end of the inertial subrange for depths in the surface-influenced layer.

The grid frequency corresponds to a dimensionless wavenumber of 2.56 Hz/(0.10 m/s 6.4 cycles/m) = 4.0. The spectra closest to the surface (0.16 and 0.4 %) show peaks due to surface waves at this grid wavenumber and at half this wavenumber (2.0). Observed surface waves included low-wavenumber standing waves and somewhat higher-wavenumber capillary ripples generated by the flexing of the tank walls. The peak-to-trough amplitude of each of these kinds of waves was typically 0.3 mm (as visually recorded). The relative motion between the probe and the waves causes the broadening of the spectral peaks seen in figure 21. Outside of this surface-wave-contaminated band, the two spectra close to the surface can be seen to show more surface suppression than would be expected from the HG theory (see

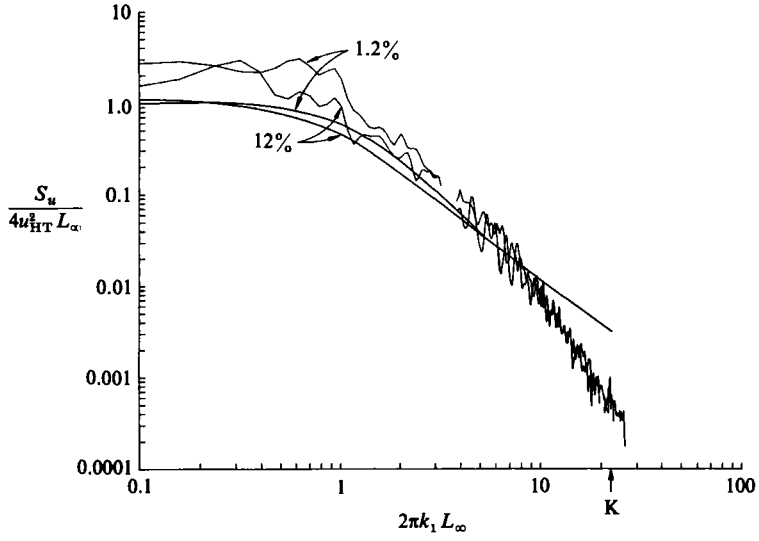

FIGURE 22. Longitudinal power spectra of horizontal velocity at 1.2 % depth (upper) and 12 % depth (lower) (12 and 120 % of L_∞, respectively) from the detailed-profile experiment. Both spectra are normalized by the spectral intercept $S_u(0) = 4u_{HT} 2L_\infty$ and breakpoint $\frac{1}{3}\pi L_\infty$ that would be expected at the surface were the surface not present. ——, Spectra predicted by the HG source theory.

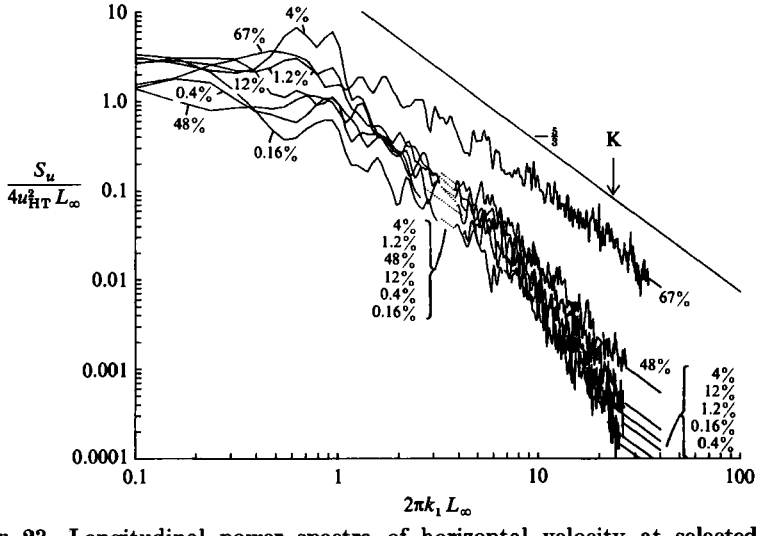

FIGURE 23. Longitudinal power spectra of horizontal velocity at selected depths from the detailed-profile experiment. Normalization as in figure 22. Depths labelled as a percentage of grid-to-surface distance z_s. K, Kolmogorov cutoff.

also figure 16). This may be a viscous-boundary-layer phenomenon, or may simply be due to the elimination of the inertial subrange at depths of the order of the Kolmogorov lengthscale.

Low-wavenumber contamination can be seen as peaks at dimensionless wavenumbers 0.16 and 0.6 (corresponding to 1 and 4 cycles/m or per turn of the probe) in these two shallow spectra. Low-wavenumber peaks at dimensionless wavenumbers 0.3 and 0.6 (2 and 4 cycles/m) are also observed in the two upper spectra from the

bulk. These were truncated before determining the turbulent velocities and integral lengthscales presented above.

Longitudinal spectra of horizontal velocity at 12 and 1.2 % relative depth are shown in figure 22. The normalization constants are the same as for the S_w spectra except for an extra factor of 2 in the ordinate since $L_u = 2L_w$ for isotropic turbulence (equation (3)). The effect of the surface is less striking on S_u than on S_w. The HG theory predicts a slight bulge in the horizontal spectra in the surface-influenced layer at dimensionless wavenumbers between 1, corresponding to the integral lengthscale, and L_∞/y, corresponding to the depth. This bulge arises from transfer of kinetic energy from the vertical velocity component that is suppressed in this wavenumber range. The measured spectra appear to have roughly the same separation as the theoretical spectra in the dimensionless wavenumber range 1–10.

More selected horizontal velocity spectra are shown in figure 23 on the same axes as figure 22. The gaps at dimensionless wavenumber 3.6 (23 cycles/m) are due to the removal of the tachometer ripple spikes. As with the high-frequency end of the vertical velocity spectra, the horizontal spectra show decay at all frequencies with distance from the grid in the bulk and nearly coincide with each other in the surface-influenced layer (compare with figure 16). Low-wavenumber peaks can be seen for a few spectra at dimensionless wavenumbers 0.6 and 0.9 (4 and 6 cycles/m). These low-wavenumber peaks seemed to occur at random with no consistent pattern (the largest happens to be for 4 % depth).

In summary, the spectra are in overall agreement with the HG predictions and confirm a relatively constant dissipation rate in the surface-influenced layer.

4. Conclusions

The results of the turbulence measurements show that a relatively simple scaling determines the structure of the turbulence in a grid-stirred tank. The surface-influenced layer scales with the integral scale which in turn depends on the distance from the grid, so this layer always occupies a fixed portion (roughly 10 %) of the space between the surface and the grid origin. The bulk region below the surface-influenced layer is characterized by a uniform turbulent Reynolds number, with integral lengthscale increasing linearly with distance from the grid, and velocity scale falling in compensating fashion. The turbulence within the surface-influenced layer, on the other hand, scales with the distance from the surface and the dissipation rate. The dissipation rate, however, itself scales with the outer scales (turbulent velocity and integral lengthscales) in the bulk in the vicinity of the surface-influenced layer.

At the moderate turbulent Reynolds numbers of these experiments, this large-scale structure (bulk and surface-influenced layer) is independent of Reynolds number, so that there are no dimensionless parameters to modify the universal dimensionless profile of any of the various turbulent quantities. This picture must be qualified by the possible presence of a Reynolds-number-dependent viscous layer very close to the surface, having a thickness smaller than that of the surface-influenced layer by a factor of order $R_L^{\frac{1}{4}}$, where R_L is the turbulent Reynolds number in the bulk.

Within the surface-influenced layer, most of the portion of the turbulent kinetic energy due to vertical velocity fluctuations is contained in eddies of size roughly equal to the depth below the surface. An inertial subrange exists for eddies between this size and the Kolmogorov scale. The larger eddies are suppressed in the sense that they can only approach to within one eddy-size of the surface. Even so, the large-scale eddies have a major influence on the near-surface hydrodynamics. They contain the

bulk of the turbulent kinetic energy throughout the surface-influenced layer, mainly in the horizontal components. Being the most persistent, they dominate phenomena associated with surface divergence straining, such as the stretching of horizontal vortex lines (Hunt 1984*b*) and the vertical transport of scalars (Brumley & Jirka 1987).

To first order, the experimental data followed the theoretical profiles of HG when scaled by the velocity and lengthscales in the bulk as predicted from the work of HT and TT, respectively. The data revealed some minor differences that are probably due to dynamic effects not adequately accounted for in the purely kinematic HG source theory. One difference was the appearance in both the vertical and horizontal velocity-fluctuation profiles of a thin boundary layer of reduced fluctuation intensity of roughly the thickness that would be expected from viscous effects. The mechanism maintaining this boundary layer is uncertain. Another difference is spectral anisotropy extending to higher wavenumbers than predicted by the HG theory. This anisotropy could be caused by the straining of inertial-scale eddies by large-scale eddies.

Grid-stirred tanks are prone to relatively steady large-scale circulations that can lead to a horizontally inhomogeneous distribution of turbulence and cause uncertainty in integral-lengthscale measurements, even though they comprise only a minor fraction of the total kinetic energy. Such circulations are not unique to grid-stirred tanks, of course, and can cause similar problems in channels, often leading to a systematic overestimation of integral lengthscales (e.g. Brumfield 1977). These problems can be overcome, however, by careful spectral-domain data analysis and by spatial and ensemble averaging as well as averaging over varying experimental conditions.

Grid-stirred tank experiments have a number of attractive features. The turbulence source is relatively far removed from the surface (roughly 10 integral lengthscales) compared with shear-flow or convective turbulence sources, so that the region of interest is not affected by the details of the generation mechanism. The turbulence is nominally homogeneous and isotropic in the horizontal plane (with the above caveat) and is not far from being isotropic (in the bulk) in any vertical plane.

The authors are grateful for helpful discussions with W. Brutsaert throughout the investigation. This study was supported by the National Science Foundation through grant CEE-8004621.

Appendix

The calculation by Hunt & Graham (1978) of velocity spectra and turbulent velocity profiles in the surface 'source-layer' of isotropic homogeneous turbulence is based upon the dimensionless von Kármán spectrum tensor:

$$\Phi_{ij} = g_3(K_m K_m \delta_{ij} - K_i K_j)(g_2 + K_m K_m)^{-\frac{17}{6}}, \tag{A 1}$$

where K_i is the i-component of the dimensionless wavenumber vector (radians per integral lengthscale), and g_2 and g_3 are constants:

$$g_2 = \pi[\Gamma(\tfrac{5}{6})/\Gamma(\tfrac{1}{3})]^2 = 0.558, \tag{A 2}$$

$$g_3 = (\tfrac{55}{36})\, g_2^{\frac{1}{2}} \pi^{-2} = 0.095. \tag{A 3}$$

Numerical approximations to the velocity-fluctuation and integral-lengthscale

profiles predicted by the HG theory have been created as an aid to computing the theoretical curves plotted in the figures of §3 to which our experimental results are compared. These *ad hoc* expressions approach the exact profiles only to the lowest order for large and small values of Y, but they provide remarkably good fits over all Y (roughly $\pm 1\%$ of full scale) for such simple forms. The expressions and numerically fit parameters for these approximate profiles are given here:

Vertical velocity-fluctuation profile:

$$\frac{w'^2}{w'^2_\infty} = [(\lambda_2 Y^2_3)^{-p} \exp[-(g^{\frac{1}{2}}_2 Y)] + 1]^{-1/p}, \tag{A 4}$$

where $p = 1.54$, $\lambda_2 = 1.4$, $g_2 = 0.558$ (equation (A 2)), and $Y = y/L_\infty$ is the depth normalized by the longitudinal integral scale far from the surface.

Horizontal velocity-fluctuation profile:

$$\frac{u'^2}{u'^2_\infty} = 1.5 - \tfrac{1}{2}[(2\lambda_1 Y^{\frac{4}{3}})^{-p} \exp[-(g^{\frac{1}{2}}_2 Y)] + (1 + 2\lambda_3 Y^{-\frac{7}{2}} \exp[-(g^{\frac{1}{2}}_2 Y)])^{-p}]^{-1/p}, \tag{A 5}$$

where $p = 0.575$, $\lambda_1 = 2.67$, $\lambda_3 = 0.522$ (see HG), and $g_2 = 0.558$ (equation (A 2)).

Transverse (vertical) integral-lengthscale profile:

$$\frac{2L_w}{L_\infty} = \left[\left(\frac{2\pi\gamma}{\lambda_2} Y\right)^{-p} \exp[-(g^{\frac{1}{2}}_2 Y)] + 1\right]^{-1/p}, \tag{A 6}$$

where $p = 0.63$, $\gamma = 0.88$ (Hunt 1984*b*), $\lambda_2 = 1.4$ (HG), and L_∞ is the far-field longitudinal integral lengthscale.

Longitudinal (horizontal) integral lengthscale:

$$\frac{L_u}{L_\infty} = \left(\frac{u'^2}{u'^2_\infty}\right)^{-1}, \tag{A 7}$$

where u'^2/u'^2_∞ is given by (A 5).

REFERENCES

Brown, L. C. 1970 Oxygen transfer in open channel flow. Ph.D. thesis, University of Wisconsin.

Brumfield, L. K. 1977 Turbulence and mass transfer (gas absorption) for flow in a rotating, annular, open channel with a stationary bottom. Ph.D. thesis, Purdue University.

Brumley, B. H. 1984 Near-surface turbulence and associated gas transfer in a grid-stirred tank. Ph.D. thesis, Cornell University.

Brumley, B. H. & Jirka, G. H. 1987 Air–water transfer of slightly soluble gases: Turbulence, interfacial processes and conceptual models. *J. Phys.-Chem. Hydrodyn.* (submitted).

Dickenson, S. C. & Long, R. R. 1978 Laboratory study of the growth of a turbulent layer of fluid. *Phys. Fluids* **21**, 1698–1701.

Dickey, T. D., Hartman, B., Hammond, D. & Hurst, E. 1984 A laboratory technique for investigating the relationship between gas transfer and fluid turbulence. In *Gas Transfer at Water Surfaces* (ed. W. Brutsaert & G. H. Jirka), pp. 93–100. D. Reidel.

E, X. & Hopfinger, E. J. 1986 On mixing across an interface in stably stratified fluid. *J. Fluid Mech.* **166**, 227–244.

Hopfinger, E. J. & Toly, J.-A. 1976 Spatially decaying turbulence and its relation to mixing across density interfaces. *J. Fluid Mech.* **78**, 155–175.

Hunt, J. C. R. 1984*a* Turbulent structure and turbulent diffusion near gas-liquid interfaces. In *Gas Transfer at Water Surfaces* (ed. W. Brutsaert & G. H. Jirka), pp. 67–82. D. Reidel.

Hunt, J. C. R. 1984*b* Turbulence structure in thermal convection and shear-free boundary layers. *J. Fluid Mech.* **138**, 161–184.

HUNT, J. C. R. & GRAHAM, J. M. R. 1978 Free-stream turbulence near plane boundaries. *J. Fluid Mech.* **84**, 209–235.

LONG, R. R. 1978 Theory of turbulence in a homogeneous fluid induced by an oscillating grid. *Phys. Fluids* **21**, 1887–1888.

MCDOUGALL, T. J. 1979 Measurements of turbulence in a zero-mean-shear mixed layer. *J. Fluid Mech.* **94**, 409–431.

RADER, C. M. 1970 An improved algorithm for high-speed autocorrelation with applications to spectral estimation. *IEEE Trans. on Audio and Electroacoustics AU-18*, pp. 439–441.

TENNEKES, H. & LUMLEY, J. L. 1972 *A First Course in Turbulence.* The MIT Press.

THOMAS, N. H. & HANCOCK, P. E. 1977 Grid turbulence near a moving wall. *J. Fluid Mech.* **82**, 481.

THOMPSON, S. M. & TURNER, J. S. 1975 Mixing across an interface due to turbulence generated by an oscillating grid. *J. Fluid Mech.* **67**, 349–368.